Electrical and thermal generation of spin currents by magnetic bilayer graphene

Ghiasi, Talieh S.; Kaverzin, Alexey A.; Dismukes, Avalon H.; de Wal, Dennis K.; Roy, Xavier; van Wees, Bart J.

Published in:
Nature Nanotechnology

DOI:
10.1038/s41565-021-00887-3

Publication date:
2021

ARTICLES
https://doi.org/10.1038/s41565-021-00887-3
nature nanotechnology

Check for updates

Electrical and thermal generation of spin currents by magnetic bilayer graphene

Talieh S. Ghiasi[1]✉, Alexey A. Kaverzin[1], Avalon H. Dismukes[2], Dennis K. de Wal[1], Xavier Roy[2] and Bart J. van Wees[1]

Ultracompact spintronic devices greatly benefit from the implementation of two-dimensional materials that provide large spin polarization of charge current together with long-distance transfer of spin information. Here spin-transport measurements in bilayer graphene evidence a strong spin–charge coupling due to a large induced exchange interaction by the proximity of an interlayer antiferromagnet (CrSBr). This results in the direct detection of the spin polarization of conductivity (up to 14%) and a spin-dependent Seebeck effect in the magnetic graphene. The efficient electrical and thermal spin-current generation is the most technologically relevant aspect of magnetism in graphene, controlled here by the antiferromagnetic dynamics of CrSBr. The high sensitivity of spin transport in graphene to the magnetization of the outermost layer of the adjacent antiferromagnet, furthermore, enables the read-out of a single magnetic sublattice. The combination of gate-tunable spin-dependent conductivity and Seebeck coefficient with long-distance spin transport in a single two-dimensional material promises ultrathin magnetic memory and sensory devices based on magnetic graphene.

Memory technology has been revolutionized by the discovery of the giant magnetoresistance[1,2] and spin-transfer torque effects[3,4], which arise from the efficient coupling of charge and spin currents in ferromagnetic materials. The spin–charge coupling is a crucial aspect of magneto-electronic devices, namely spin valves that consist of two layers of ferromagnetic materials separated by a non-magnetic layer, in which altering the relative magnetization orientation of the layers results in a substantial change in resistance[5]. Such spin valves can be designed in the two-dimensional (2D) limit owing to the recent emergence of 2D magnetic materials[6,7] in the architecture of van der Waals (vdW) heterostructures in which exceptional functionalities are achieved by integrating the properties of the individual layers[8].

Furthermore, most spintronic applications require the strong spin–charge coupling in the 2D magnetic materials to be accompanied with a long-distance transfer of the spin information. In this regard, graphene is a superior choice with its high charge carrier mobility as the absence of hyperfine interactions and small intrinsic spin–orbit coupling (SOC) allow for a long spin lifetime[9–11]. The proximity of other materials to graphene can efficiently modulate its band structure and induce considerable SOC[12,13] and exchange interaction[14–18], which are essential for spin generation and manipulation. In particular, the proximity effect of 2D magnetic materials would bring the technology of ultrathin spin-logic devices to the limit when the magnetic behaviour of an individual atomic layer directly controls the long-distance information transfer by the spins in the neighbouring graphene layer.

The experimental realization of the proximity-induced exchange interaction in graphene has been reported, and observed as Shubnikov de-Haas oscillations and the Zeeman spin Hall effect[19–21], anomalous Hall effect (AHE)[22,23] and the Hanle precession of injected spins by the induced exchange field ($\mathbf{B}_{exch}$)[24–27]. Among them, the latter is the most unambiguous and reliable approach when spin-sensitive Co electrodes are used to directly detect the modulation of the spin signal by the $\mathbf{B}_{exch}$. However, so far Hanle precession measurements in graphene have shown a rather weak exchange interaction, which only leads to an additional precession of the spins around the $\mathbf{B}_{exch}$. Even though all these experimental reports so far have shown evidence for an induced $\mathbf{B}_{exch}$, the active generation of spin currents by graphene both electrically and thermally, as the most technologically relevant aspect of the induced magnetism, has not been addressed yet.

In this work, we detected the spin polarization of conductivity together with the spin-dependent Seebeck effect (SDSE) in bilayer graphene proximity coupled to 2D interlayer antiferromagnetic (AFM) CrSBr. The spin-transport measurements directly address the conductivity in graphene, and show a strong spin polarization up to 14%, which is as large as that in metallic ferromagnets. This is evidenced by the efficient electrical and thermal generation of spin currents by the magnetic graphene, up to the magnetic transition temperature of CrSBr. These observations, together with AHE measurements, promise major advances in 2D spintronic/spin-caloritronic circuitry. Additionally, they give insight into the magnetic nature of graphene, controlled by the AFM dynamics of CrSBr.

The strong exchange interaction results in a considerable spin splitting (Δ) of the graphene band structure. The resulting substantial difference in the density of charge carriers (n) with spin parallel ($\uparrow$) and antiparallel ($\downarrow$) to the $\mathbf{B}_{exch}$ (Fig. 1a) leads to the spin-dependent conductivity. The spin polarization of conductance in graphene (P_{Gr}) is expected to be efficiently tunable by shifting the position of the Fermi energy (E_F) with a gate electric field (as proposed in Fig. 1b), and to reach the maxima of its absolute value when the density of any of the two carrier types is minimal. Such an efficient gate tunability of the spin polarization of conductivity is the basis for all-electric spin field-effect transistors in spin-logic circuitries[28]. The use of bilayer graphene is particularly encouraged, as it can allow for gate tunability of the exchange splitting[29–32].

Most of the explored 2D magnetic materials, however, suffer from extreme air instability and the low temperature of magnetic

[1]Zernike Institute for Advanced Materials, University of Groningen, Groningen, the Netherlands. [2]Department of Chemistry, Columbia University, New York, NY, USA. ✉e-mail: t.s.ghiasi@rug.nl

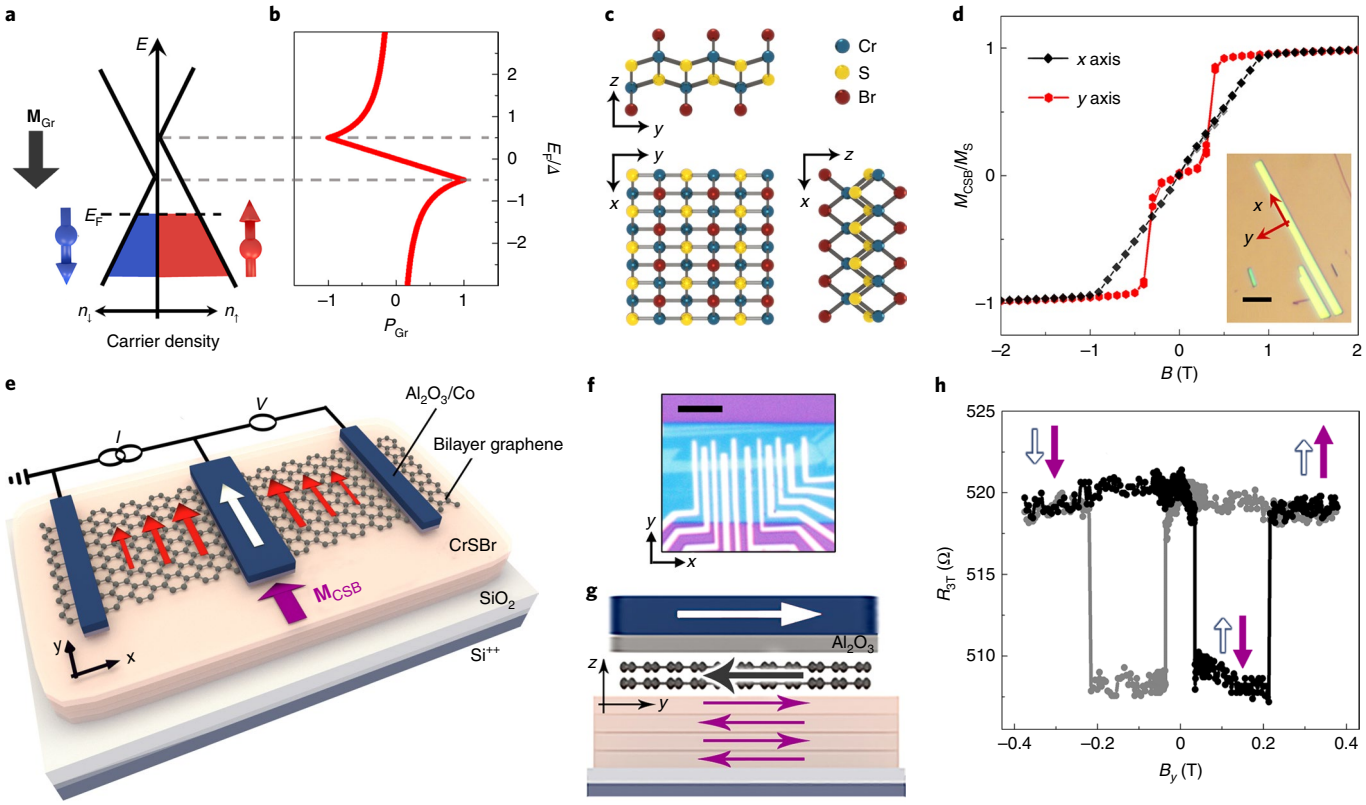

Fig. 1 | Induced magnetism in bilayer graphene by the proximity of CrSBr. a, Spin-dependent density of charge carriers ($n_\uparrow$ and $n_\downarrow$) versus energy of bilayer graphene (Gr) in the proximity of CrSBr, with the spin-splitting Δ caused by the exchange interaction. Δ is considered to be constant for the conduction and valence bands. $\mathbf{M}_{Gr}$, shown by the black arrow, is assumed to be aligned with spin down. **b**, Dependence of the spin polarization of graphene conductivity P_{Gr} on the Fermi energy position E_F, under the assumptions of the Drude model (Supplementary Section 11). **c**, Side and top views of the CrSBr crystal structure. **d**, Magnetization of a bulk CrSBr single crystal ($\mathbf{M}_{CSB}$) versus external magnetic field ($\mathbf{B}$), measured using SQUID magnetometry at $T = 30$ K along the x and y directions of the crystal. M_{CSB} is normalized to the saturation magnetization (M_s) value taken at $B = 3$ T. The SQUID measurement along the hardest magnetic z axis is shown in Supplementary Section 14. Inset: an optical micrograph of typical CrSBr flakes, exfoliated on the SiO_2 substrate. Scale bar, 5 μm. **e**, Schematics of a 3T spin valve measurement geometry, showing a bilayer graphene/bulk CrSBr heterostructure and ferromagnetic electrodes (Al_2O_3/Co). The white and purple arrows represent the magnetizations of the Co electrode and CrSBr (top-most layer), respectively. Spin injection by the Co, together with spin-current generation by the magnetic graphene, result in an accumulation of spin-up electrons (red arrows) under the given alignment of $\mathbf{M}_{Co}$ and $\mathbf{M}_{CSB}$, with $P_{Gr} > 0$ and $P_{Co} < 0$. **f**, Optical micrograph of device D1, fabricated with a vdW stack of bilayer graphene and CrSBr (~20 nm) and Al_2O_3(0.8 nm)/Co(30 nm) electrodes. Scale bar, 5 μm. **g**, Side-view sketch of the spin-valve device, showing a magnetization configuration of $\mathbf{M}_{Co}$ (white), $\mathbf{M}_{Gr}$ (black) and $\mathbf{M}_{CSB}$ (purple). **h**, Independent switching of the $\mathbf{M}_{Co}$ and $\mathbf{M}_{CSB}$ (and so $\mathbf{M}_{Gr}$) under an external magnetic field along the y axis (B_y) leads to the unconventional spin-valve measurements in the 3T geometry with the distinct levels of the 3T resistance $R_{3T} = V/I$ (also see Supplementary Section 3). The black curve is the R_{3T} measurement starting at $B_y = -0.4$ T (trace) and the grey curve is the retrace measurement, starting at $B_y = +0.4$ T. The white and purple arrows show the $\mathbf{M}_{Co}$ and $\mathbf{M}_{CSB}$ magnetization configurations for the trace measurement. The change in R_{3T} versus B_y is proportional to P_{Gr}, $\Delta R_{3T} \propto P_{Gr}$ (Supplementary Section 6). The 3T measurement is performed at $T = 4.5$ K, with $I = 5$ μA.

transitions[33]. Here we tackled this obstacle by utilizing the recently explored CrSBr 2D crystal (Fig. 1c), which is an air-stable vdW semiconductor (bandgap of ~1.5 eV; see Supplementary Section 18 for transport measurements) with an interlayer AFM ordering up to a relatively high Néel temperature of $T_N \approx 132$ K (refs. [34–37]). Furthermore, the antiferromagnetism promises ultrafast operations and robustness against external magnetic fields[38] and also is expected to be tunable by a gate electric field[35,39]. Mechanical cleavage of the CrSBr crystal results in flakes with a specific rectangular geometry that correlates with its in-plane magnetic anisotropy axes (Fig. 1d inset). The behaviour of CrSBr magnetization ($\mathbf{M}_{CSB}$) measured versus an external magnetic field ($\mathbf{B}$) using a superconducting quantum interference device (SQUID) magnetometer (Fig. 1d) displayed a sharp modulation of $\mathbf{M}_{CSB}$ when $\mathbf{B}$ was applied along the y axis. This corresponds to the AFM behaviour with a spin–flip transition at an applied magnetic field of $B_{M,y} \sim 0.2$ T (at which $\mathbf{M}_{CSB}$ switches along the y axis) and defines the y direction as the in-plane magnetic easy axis. In contrast, along the x direction, M_{CSB} increased gradually with a much higher saturation field ($B_{M,x} \approx 1$ T). This is a result of the gradual canting of the antiparallel magnetizations of the CrSBr layers towards the x direction (the in-plane magnetic hard axis). When graphene is brought on top of the CrSBr flake, the magnetic behaviour of the outermost CrSBr layer is imprinted in the graphene so that the magnetization of graphene ($\mathbf{M}_{Gr}$) is expected to be collinear with the magnetization of the outermost layer of the CrSBr flake (the alignment of $\mathbf{M}_{Gr}$ and $\mathbf{M}_{CSB}$ is further discussed in Supplementary Section 13).

Spin-dependent conductivity. The presence of spin-dependent conductivity in graphene was directly observed in the spin-valve design shown in Fig. 1e. Using the three-terminal (3T) geometry, the resistance was measured versus the magnetic field B_y, applied

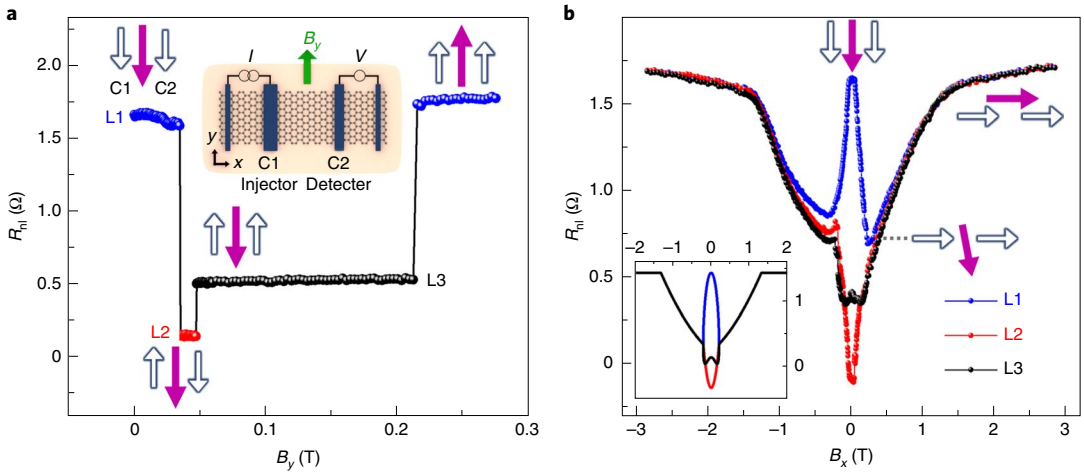

Fig. 2 | Spin transport in bilayer graphene with spin-polarized conductivity. a, Non-local spin-valve measurement. The first harmonic non-local resistance $R_{nl} = V/I$ versus B_y (with $I = 5\,\mu A$) shows three levels (L1, L2 and L3), which correspond to the different configurations of Co injector and detector magnetization directions ($\mathbf{M}_{Co}$, white arrows) with respect to the magnetization direction of CrSBr ($\mathbf{M}_{CSB}$, purple arrow). Inset: schematic of the non-local measurement geometry under the applied B_y (green arrow), with C1 and C2 Co electrodes as the spin injector and detector, respectively. For the measurements in the reciprocal geometry and with the other Co detectors, see Supplementary Sections 2 and 15. **b**, Modulation of R_{nl} as a function of B_x, measured in Hanle geometry with the initial alignment of $\mathbf{M}_{Co}$ of the injector and detector and $\mathbf{M}_{CSB}$ (which correspond to L1, L2 and L3, respectively, as defined in **a**). The asymmetry in the Hanle curves could be related to the possible few-degrees misalignment of the magnetization axes of the Co electrodes with respect to that of the CrSBr crystal and/or misalignment of **B** from the *x* axis. Inset: Hanle curves calculated by the spin-dependent graphene conductivity model. The best fit to the measured results is provided given that $P_{Gr} \approx 14\%$ and $P_{inj} \approx P_{det} \approx -24\%$ (Supplementary, Section 9). All the measurements were performed at $T = 4.5$ K.

along the easy axes of the Co electrodes and the CrSBr crystal. As shown in Fig. 1g, in the spin-valve heterostructure of Co/Al_2O_3/magnetic graphene, the relative orientation of $\mathbf{M}_{Gr}$ with respect to $\mathbf{M}_{Co}$ defines the spin polarization of the injected current and therefore considerably changes the resistance of the contact between graphene and Co (R_{3T}). The abrupt change in resistance (Fig. 1h), which depends on the relative orientation of $\mathbf{M}_{Gr}$ and $\mathbf{M}_{Co}$, resembles the giant magnetoresistance effect, but with the advantage of a long-distance spin transfer in the graphene. This would not happen in a conventional 3T measurement with a non-magnetic graphene, because when the Co magnetization is reversed both spin injection and detection simultaneously change sign, which results in no magnetoresistance[40]. Therefore, the observation of the 3T spin-valve effect is only possible if the graphene is magnetic, with a non-zero spin polarization of conductance P_{Gr}.

The spin–charge current coupling in graphene was further studied by measuring the pure spin current generated by the magnetized graphene in a non-local four-terminal (4T) geometry (Fig. 2a), in which the charge current path can be fully separated from the voltage detection circuit. The non-local resistance ($R_{nl} = V/I$) is measured versus B_y. In an equivalent measurement on pristine graphene, one would observe two (non-local) resistance levels associated with the parallel and antiparallel magnetization alignment of the injector and detector Co electrodes[9]. In contrast, here we observed three resistance levels that are only possible if the spin transport in graphene depends on the relative orientation of $\mathbf{M}_{Gr}$ (or $\mathbf{M}_{CSB}$) with respect to the magnetization of the injector $\mathbf{M}_{Co,inj}$ and that of the detector $\mathbf{M}_{Co,det}$ electrodes. The spin-valve measurement was performed with an initial alignment of all three magnetic elements (injector, detector and CrSBr) at $B_y = -1$ T. By increasing the field B_y from 0 T, the magnetizations of the injector and the detector electrodes switched to the opposite direction one after the other at $B_y \lesssim 50$ mT. The third switch (at $B_y \approx 0.21$ T) happened at a value of the field that is too large to be related to the Co electrodes, given their geometrical anisotropy. However, it corresponds well with switching field of the $\mathbf{M}_{CSB}$ along its easy axis (shown in the SQUID magnetometry of Fig. 1d), which directly confirms the non-zero spin polarization of the graphene conductivity as a result of the proximity-induced magnetism.

The spin polarization in graphene is defined as $P_{Gr} = (\sigma_u - \sigma_d)/(\sigma_u + \sigma_d)$, where σ_u and σ_d are conductivities for spin-up and spin-down channels. Solving the spin-charge coupled diffusive transport equations (Supplementary Section 5), we derived the non-local resistance as:

$$R_{nl} = \frac{\lambda R_{sq}}{2W} e^{-L/\lambda}(P_{inj} - P_{Gr})(P_{det} - P_{Gr}) \quad (1)$$

where P_{inj} and P_{det} are the spin polarizations of the injector and detector contacts and λ, R_{sq}, L and W are the spin relaxation length, square resistance, length and width, respectively, of the graphene channel (in between the injector and detector contacts). The above expression can be expanded as:

$$R_{nl} \propto P_{inj}P_{det} - P_{Gr}P_{det} - P_{inj}P_{Gr} + P_{Gr}P_{Gr} \quad (2)$$

The $P_{inj}P_{det}$ term corresponds to a spin signal injected/detected via ferromagnetic injector/detector contacts. $P_{inj}P_{Gr}$ is due to the spin injection via ferromagnetic contact, but the non-local signal is detected as a charge voltage that builds up because of the spin-to-charge conversion that happens in graphene itself and $P_{Gr}P_{det}$ corresponds to the reciprocal effect. Finally, $P_{Gr}P_{Gr}$ is due to the spin signal that is both generated and detected by graphene itself. The presence of the last term implies that, in principle, spin polarized contacts are not required to observe the charge–spin current coupling. However, it might not be possible to differentiate it from a spurious background under an applied **B** when only non-magnetic electrodes are used. Here we estimated λ to be about 630 nm and obtained the polarizations as $P_{Gr} \approx 14\%$ and $P_{inj} \approx P_{det} \approx -24\%$ (Supplementary Sections 4–10). Having the P_{Gr}, we roughly estimated the exchange splitting to be $\Delta = 2E_F P_{Gr} \approx 20$ meV, which corresponds to $B_{exch} \approx 170$ T, assuming E_F to be the same

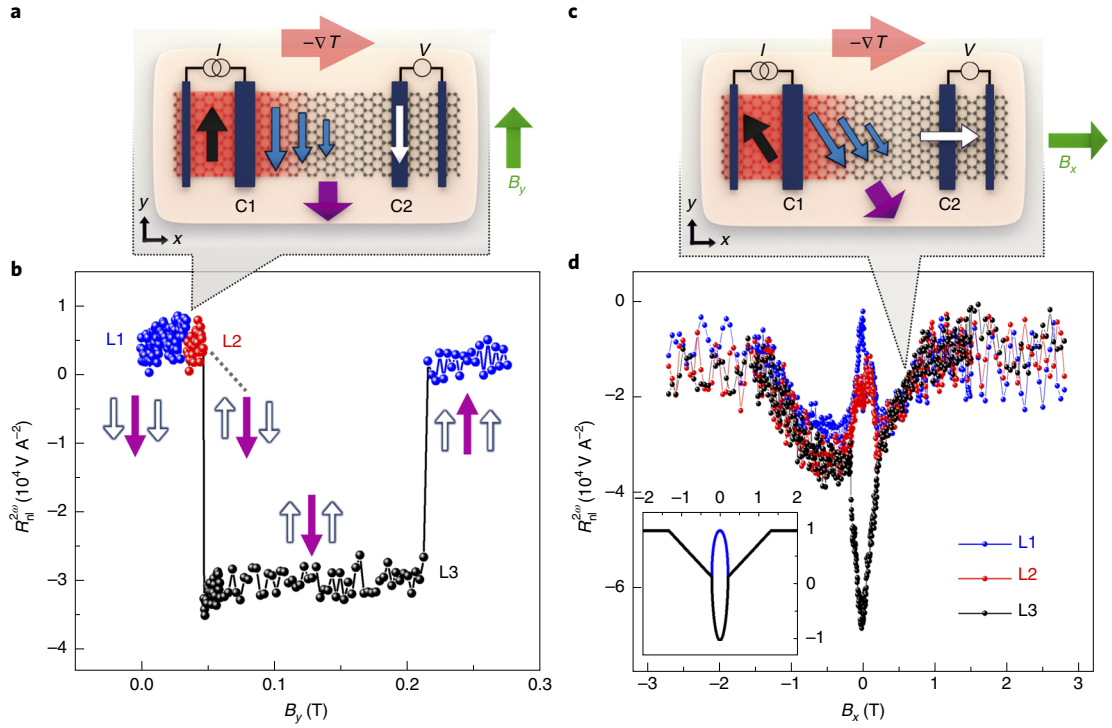

Fig. 3 | SDSE in the magnetized bilayer graphene. a, The schematic of the non-local measurement geometry shows a temperature gradient (∇T) in the graphene channel due to Joule heating at the current-source contacts that results in the thermal generation of a spin current due to the finite P_{Gr}. The sketch shows the initial alignment of $\mathbf{M}_{CSB}$ (purple arrow) and $\mathbf{M}_{Co,det}$ (white arrow) with respect to the magnetic field (green arrow), which corresponds to L1 or L2. In this case, $\mathbf{M}_{Gr}$ (black arrow) is pointing up (along the *y* axis) and there is an accumulation of spin downs (blue arrows) close to the hot region. **b**, Second harmonic non-local spin-valve measurement of $R_{nl}^{2\omega} = V^{2\omega}/I^2$ versus B_y. The different magnetization configurations of $\mathbf{M}_{Co}$ and $\mathbf{M}_{CSB}$ are shown, which correspond to L1, L2 and L3. **c**, Device sketch with the magnetization configuration of $\mathbf{M}_{CSB}$ and $\mathbf{M}_{Co,det}$ under the applied $B_x > 0.2$ T (saturation field of Co along the *x* axis) showing a gradual tilt of the $\mathbf{M}_{CSB}$ and the thermally generated spins towards B_x. **d**, Modulation of the $R_{nl}^{2\omega}$ as a function of B_x in the Hanle geometry. Inset: theoretically calculated Hanle curves for the second harmonic signal, given that SDSE is the spin generating mechanism (Supplementary Section 12). All the measurements were performed at $T = 4.5$ K.

as that in device D3 (Supplementary Section 11). Note that in an electron-doped device D2 (Supplementary Section 17), we observed an opposite sign for P_{Gr} as compared with that in device D1. This is an indication of the possible gate tunability of the spin polarization of conductivity in graphene, consistent with Fig. 1b.

The modulation of the spin signal under the magnetic field B_x applied in-plane, perpendicular to the Co and CrSBr easy axes, further confirms the presence of the very large $\mathbf{B}_{exch}$ in the graphene (Fig. 2b). We label this experiment a Hanle measurement as a generalized term, as the effect of the $\mathbf{B}_{exch}$ on the spins is similar to that of an external field. In this system, the precession is governed by the $\mathbf{B}_{exch}$ as its magnitude is much larger than the B_x. The B_x controls the directions of $\mathbf{M}_{Co}$ and $\mathbf{M}_{CSB}$ (or $\mathbf{B}_{exch}$) by pulling them towards the *x* axis with saturation fields of $B_{Co} \approx 0.2$ T and $B_{CSB} \approx 1.3$ T. The Hanle curves in Fig. 2b are measured after the initial alignment of the $\mathbf{M}_{Co}$ and $\mathbf{M}_{CSB}$ along the *y* axis, which sets the magnetization configuration that corresponds to L1, L2 or L3 (as labelled in Fig. 2a). The B_x is applied perpendicular to the initial direction of the injected spins. For L1, the R_{nl} has its maximum value at $B_x = 0$ T, as the injected spins are aligned with the $\mathbf{B}_{exch}$. Once the B_x pulls the $\mathbf{M}_{Co}$ along the *x* direction, the strong $\mathbf{B}_{exch}$ fully randomizes the component of the injected spins that are perpendicular to it. At $B_x \approx 0.2$ T, the magnetization directions of the contacts are saturated along the *x* axis while $\mathbf{B}_{exch}$ is still mostly pointing along the *y* axis. This yields to only a small projection of the injected spins in the direction of $\mathbf{B}_{exch}$, and thus results in a considerable decay of R_{nl}. The increase to $B_x > 0.2$ T pulls the $\mathbf{M}_{CSB}$ further along the *x* direction with saturation at 1.3 T. When the $\mathbf{M}_{CSB}$ aligns with $\mathbf{M}_{Co}$ once again, the R_{nl} retrieves its initial value. The Hanle curves measured for the antiparallel alignment of $\mathbf{M}_{CSB}$ with respect to $\mathbf{M}_{Co,inj}$ or $\mathbf{M}_{Co,det}$ (which correspond to configurations L2 or L3 in Fig. 2a) also show a similar behaviour, but with the distinct initial value of R_{nl} at $B_x = 0$ T. Overall, the behaviour of the spin signal in the Hanle curves is determined by the relative orientation of the $\mathbf{M}_{Co}$ and $\mathbf{M}_{Gr}$ as the very large $\mathbf{B}_{exch}$ allows for the information transfer only by the spins collinear to the $\mathbf{M}_{Gr}$. The Fig. 2b inset shows the Hanle curves derived from the analytical expression for the R_{nl} (Supplementary Section 8), which agree well with the experimental results.

Spin-dependent Seebeck effect. The strong induced magnetism in graphene also led to the observation of a SDSE[41,42]. Owing to the spin dependence of the Seebeck coefficient, we could generate spin current by having a thermal gradient in the magnetized graphene channel (Fig. 3a). We measured the second harmonic signal associated with thermal effects due to Joule heating ($\Delta T \propto I^2$). Figure 3b shows that the non-local second harmonic resistance ($R_{nl}^{2\omega} = V^{2\omega}/I^2$, where ω is the frequency of the source current) abruptly changes with the switch of the detector magnetization direction (at $B_y \approx 50$ mT), which becomes antiparallel to the CrSBr magnetization. The spin signal retrieves its initial value when $\mathbf{M}_{CSB}$ also switches (at ≈ 0.21 T) and becomes parallel to $\mathbf{M}_{Co,det}$ again. We observed that the switch in the direction of the injector magnetization at $B_y \approx 35$ mT did not change the $R_{nl}^{2\omega}$. This assures the thermal origin of the measured spin signal that is generated only by the Joule heating of graphene at the injector contact, independent of the injector magnetization. In Fig. 3c,d, we demonstrate the modulation of the SDSE spin signal

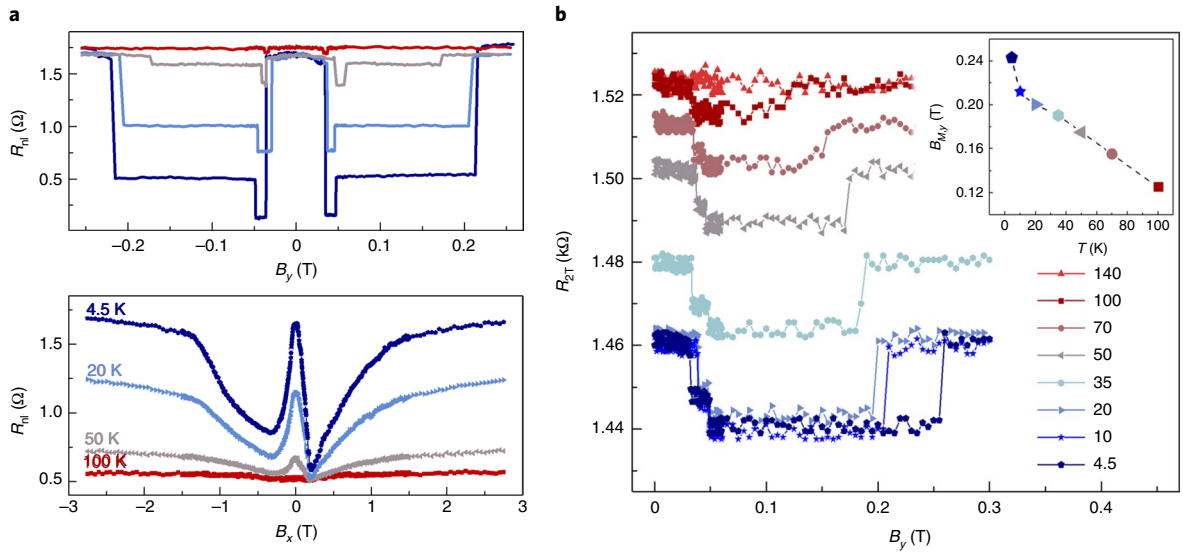

Fig. 4 | Temperature dependence of the spin signal. a, The non-local spin-valve (top) and Hanle (bottom) measurements at various temperatures. The Hanle curves were measured with the parallel initial configuration of $\mathbf{M}_{CSB}$, $\mathbf{M}_{Co,inj}$ and $\mathbf{M}_{Co,det}$. The measured spin-valve data are shifted along the *y* axis of the plot for a clearer demonstration (see Supplementary Fig. 4 for the R_{nl} shown without the offset). **b**, Two-terminal resistance (R_{2T}) measured between contacts C1 and C2 versus B_y at various temperatures (K). Inset: the gradual decay in the switching field of CrSBr along its easy axis ($B_{M,y}$) by the increase in temperature.

versus B_x measured for the different magnetization configurations of the injector, detector and CrSBr (defined for L1, L2 and L3 in Fig. 3b). The modulation of the $R_{nl}^{2\omega}$ versus B_x is understood given the collinearity of the thermally injected spins with the magnetization of graphene, consistent with theoretically calculated curves shown in the inset of Fig. 3d (also see Supplementary Section 12). The similar behaviour of the second harmonic L1 and L2 Hanle curves further confirms that $\mathbf{M}_{Co,inj}$ has no influence on the detected signal.

Magnetic phase transition. The generation of the spin currents by the magnetized graphene should persist up to the relatively high Néel temperature of CrSBr ($T_N \approx 132$ K). We examined this by the local and non-local spin transport measurements at various temperatures (Fig. 4). The dependence of the spin signal on temperature reflects the temperature dependence of the magnetization of CrSBr layers. The spin-valve and Hanle curves, measured non-locally up to $T = 100$ K (Fig. 4a), show a substantial decay of the spin signal. This is further confirmed by the two-terminal measurements plotted in Fig. 4b. The considerable spin polarization of graphene allows for the detection of large spin signals in the local two-terminal geometry, which shows three resistance levels that correspond to the magnetization switch of contact C1, C2 and CrSBr. Consistent with the non-local measurements, the size of the spin-valve switches decreases with a rise in temperature and fully vanishes (below the noise level) at $T > 100$ K. Such a decay is attributed to the randomization of the magnetization of CrSBr and suppression of the induced magnetism in graphene, as the decay is much larger than that expected from the temperature dependence of Co spin polarization or spin transport in graphene on non-magnetic substrates[11,43]. Moreover, we observed that, as the temperature increases, $B_{M,y}$ shifts towards smaller values (Fig. 4b inset), consistent with the temperature dependence of the SQUID magnetometry of CrSBr[36].

Anomalous Hall effect. The induced magnetism in graphene, if accompanied with SOC, is expected to result in the emergence of AHE[44]. We assessed this by interfacing a thin exfoliated CrSBr bulk flake with a graphene Hall bar (Fig. 5a) and measuring the transverse voltage (V_{xy}) as a function of the out-of-plane magnetic field (B_z) when a longitudinal current was applied. The B_z gradually pulled the $\mathbf{M}_{CSB}$ out of the 2D plane, which led to an imbalance in the density of the out-of-plane spins. The AHE introduces a sizable non-linearity in the B dependence of the transverse resistance R_{xy}. The subtraction of the ordinary Hall effect (linear in B) provides us with the solitary contribution of the AHE (R_{AHE}) that fully saturates at $B_z \approx 4$ T, shown for various gate voltages in Fig. 5b. The strength of the AHE depends on the position of the E_F in the band structure of the magnetized graphene. Figure 5c shows an increase in the extracted non-linearity of the Hall voltage as the E_F approaches the charge neutrality point and preserves the sign for both electrons and holes. Note that the possible presence of the electron–hole puddles can contribute to the non-linearity of the Hall voltage when the E_F is close to the charge neutrality point in a non-homogeneous graphene channel[45]. The observation of the AHE not only confirms the induced magnetism but also indicates an enhanced SOC in the graphene that allows for the emergence of additional spin-to-charge conversion mechanisms (for example, spin Hall or Rashba–Edelstein effects)[46].

Conclusions

These findings present the air-stable graphene/CrSBr vdW heterostructure as an exceptional platform for addressing a broad range of spin-dependent phenomena[5,11] and quantum effects in magneto-electronic devices[47,48] because the magnetism, SOC and long spin lifetime are brought together in a single 2D lattice. The direct measurement of the strong spin-polarized conductance in graphene in the proximity of an antiferromagnet ensures its applications for the prospective 2D memory technology with an ultrafast operation and the long-distance transfer of spin information. In magnetic tunnel junctions, for instance, the generated spin currents by the magnetic graphene can be used to induce a spin-transfer torque in 2D magnetic random access memories[49,50]. Moreover, graphene with a high sensitivity of charge and spin transport to the magnetization of the outermost layer of the neighbouring 2D AFM CrSBr provides a tool to study the behaviour of a single magnetic sublattice that is also promising for magnetic sensory systems.

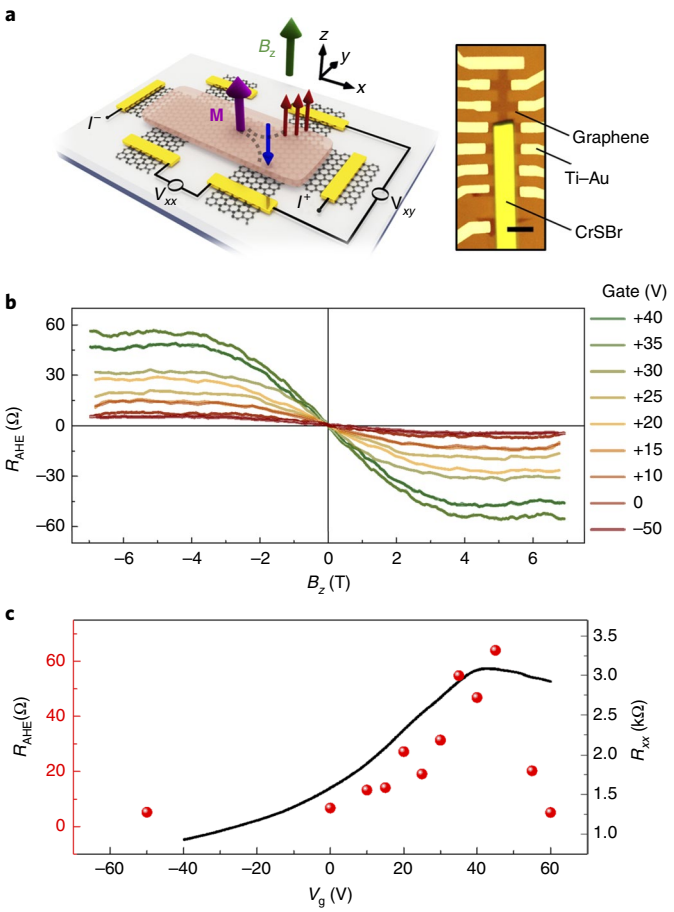

Fig. 5 | AHE in a bilayer graphene/CrSBr vdW heterostructure. a, Schematic (left) and optical micrograph (right) of device D3, which consists of a bilayer graphene Hall bar on SiO_2, partially covered with a CrSBr flake (thickness ~50 nm) with Ti(5 nm)/Au(100 nm) electrodes. Scale bar, 5 μm. The red and blue arrows represent the out-of-plane spins. **b**, The non-linear antisymmetric component of the $R_{xy} = V_{xy}/I$ as a function of an out-of-plane magnetic field (B_z), attributed to the AHE (R_{AHE}), measured at different back-gate voltages (also see Supplementary Section 19). **c**, Left axis: the magnitude of the AHE signal (defined as an average of the maximum and minimum values of the R_{AHE} at $B_z > +4$ T and < -4 T) at the various back-gate voltages V_g, shown by the red dots. Right axis: longitudinal resistance of graphene (R_{xx}) versus V_g, shown by the black line. The measurements were performed at $T = 30$ K.

The electrical and thermal generation of spin currents by the magnetized graphene grants the design of spin-logic devices without the need for magnetic injector and/or detector electrodes. This, together with the possibility for an efficient modulation of the spin-polarization of conductivity by electric fields via local (top) gates, allows for all-electric graphene-based spin-logic circuitries. These realizations, if accompanied with a large-scale growth of the vdW heterostructures and the development of the 2D magnets with a magnetic phase transition above room temperature, would lead to substantial advances in the 2D spintronics and spin-caloritronics technology.

Online content

Any methods, additional references, Nature Research reporting summaries, source data, extended data, supplementary information, acknowledgements, peer review information; details of author contributions and competing interests; and statements of data and code availability are available at https://doi.org/10.1038/s41565-021-00887-3.

Received: 24 June 2020; Accepted: 2 March 2021;
Published online: 6 May 2021

References

1. Baibich, M. N. et al. Giant magnetoresistance of (001)Fe/(001)Cr magnetic superlattices. *Phys. Rev. Lett.* **61**, 2472–2475 (1988).
2. Binasch, G., Grünberg, P., Saurenbach, F. & Zinn, W. Enhanced magnetoresistance in layered magnetic structures with antiferromagnetic interlayer exchange. *Phys. Rev. B* **39**, 4828–4830 (1989).
3. Slonczewski, J. C. et al. Current-driven excitation of magnetic multilayers. *J. Magn. Magn. Mater.* **159**, L1–L7 (1996).
4. Myers, E., Ralph, D., Katine, J., Louie, R. & Buhrman, R. Current-induced switching of domains in magnetic multilayer devices. *Science* **285**, 867–870 (1999).
5. Žutić, I., Fabian, J. & Sarma, S. D. Spintronics: fundamentals and applications. *Rev. Mod. Phys.* **76**, 323–410 (2004).
6. Gong, C. et al. Discovery of intrinsic ferromagnetism in two-dimensional van der Waals crystals. *Nature* **546**, 265–269 (2017).
7. Gong, C. & Zhang, X. Two-dimensional magnetic crystals and emergent heterostructure devices. *Science* **363**, eaav4450 (2019).
8. Geim, A. K. & Grigorieva, I. V. Van der Waals heterostructures. *Nature* **499**, 419–425 (2013).
9. Tombros, N., Jozsa, C., Popinciuc, M., Jonkman, H. T. & Van Wees, B. J. Electronic spin transport and spin precession in single graphene layers at room temperature. *Nature* **448**, 571–574 (2007).
10. Abergel, D., Apalkov, V., Berashevich, J., Ziegler, K. & Chakraborty, T. Properties of graphene: a theoretical perspective. *Adv. Phys.* **59**, 261–482 (2010).
11. Han, W., Kawakami, R. K., Gmitra, M. & Fabian, J. Graphene spintronics. *Nat. Nanotechnol.* **9**, 794–807 (2014).
12. Gmitra, M. & Fabian, J. Graphene on transition-metal dichalcogenides: a platform for proximity spin–orbit physics and optospintronics. *Phys. Rev. B* **92**, 155403 (2015).
13. Garcia, J. H., Vila, M., Cummings, A. W. & Roche, S. Spin transport in graphene/transition metal dichalcogenide heterostructures. *Chem. Soc. Rev.* **47**, 3359–3379 (2018).
14. Haugen, H., Huertas-Hernando, D. & Brataas, A. Spin transport in proximity-induced ferromagnetic graphene. *Phys. Rev. B* **77**, 115406 (2008).
15. Yang, H.-X. et al. Proximity effects induced in graphene by magnetic insulators: first-principles calculations on spin filtering and exchange-splitting gaps. *Phys. Rev. Lett.* **110**, 046603 (2013).
16. Zollner, K., Gmitra, M., Frank, T. & Fabian, J. Theory of proximity-induced exchange coupling in graphene on hBN/(Co, Ni). *Phys. Rev. B* **94**, 155441 (2016).
17. Asshoff, P. et al. Magnetoresistance of vertical co-graphene–NiFe junctions controlled by charge transfer and proximity-induced spin splitting in graphene. *2D Mater.* **4**, 031004 (2017).
18. Behera, S. K., Bora, M., Chowdhury, S. S. P. & Deb, P. Proximity effects in graphene and ferromagnetic $CrBr_3$ van der Waals heterostructures. *Phys. Chem. Chem. Phys.* **21**, 25788–25796 (2019).
19. Wei, P. et al. Strong interfacial exchange field in the graphene/EuS heterostructure. *Nat. Mater.* **15**, 711–716 (2016).
20. Wu, Y.-F. et al. Magnetic proximity effect in graphene coupled to a $BiFeO_3$ nanoplate. *Phys. Rev. B* **95**, 195426 (2017).
21. Tang, C., Zhang, Z., Lai, S., Tan, Q. & Gao, W.-b. Magnetic proximity effect in graphene/$CrBr_3$ van der Waals heterostructures. *Adv. Mater.* **32**, 1908498 (2020).
22. Wang, Z., Tang, C., Sachs, R., Barlas, Y. & Shi, J. Proximity-induced ferromagnetism in graphene revealed by the anomalous Hall effect. *Phys. Rev. Lett.* **114**, 016603 (2015).
23. Tang, C. et al. Approaching quantum anomalous Hall effect in proximity-coupled YIG/graphene/h-BN sandwich structure. *APL Mater.* **6**, 026401 (2018).
24. Leutenantsmeyer, J. C., Kaverzin, A. A., Wojtaszek, M. & Van Wees, B. J. Proximity induced room temperature ferromagnetism in graphene probed with spin currents. *2D Mater.* **4**, 014001 (2016).
25. Singh, S. et al. Strong modulation of spin currents in bilayer graphene by static and fluctuating proximity exchange fields. *Phys. Rev. Lett.* **118**, 187201 (2017).
26. Karpiak, B. et al. Magnetic proximity in a van der Waals heterostructure of magnetic insulator and graphene. *2D Mater.* **7**, 015026 (2019).
27. Cummings, A. W. Probing magnetism via spin dynamics in graphene/2D-ferromagnet heterostructures. *J. Phys. Mater.* **2**, 045007 (2019).
28. Behin-Aein, B., Datta, D., Salahuddin, S. & Datta, S. Proposal for an all-spin logic device with built-in memory. *Nat. Nanotechnol.* **5**, 266–270 (2010).

29. Michetti, P., Recher, P. & Iannaccone, G. Electric field control of spin rotation in bilayer graphene. *Nano Lett.* **10**, 4463–4469 (2010).
30. Michetti, P. & Recher, P. Spintronics devices from bilayer graphene in contact to ferromagnetic insulators. *Phys. Rev. B* **84**, 125438 (2011).
31. Zollner, K., Gmitra, M. & Fabian, J. Electrically tunable exchange splitting in bilayer graphene on monolayer $Cr_2X_2Te_6$ with X = Ge, Si, and Sn. *New J. Phys.* **20**, 073007 (2018).
32. Cardoso, C., Soriano, D., García-Martínez, N. & Fernández-Rossier, J. Van der Waals spin valves. *Phys. Rev. Lett.* **121**, 067701 (2018).
33. Gibertini, M., Koperski, M., Morpurgo, A. & Novoselov, K. Magnetic 2D materials and heterostructures. *Nat. Nanotechnol.* **14**, 408–419 (2019).
34. Göser, O., Paul, W. & Kahle, H. Magnetic properties of CrSBr. *J. Magn. Magn. Mater.* **92**, 129–136 (1990).
35. Wang, H., Qi, J. & Qian, X. Electrically tunable high Curie temperature two-dimensional ferromagnetism in van der Waals layered crystals. *Appl. Phys. Lett.* **117**, 083102 (2020).
36. Telford, E. J. et al. Layered antiferromagnetism induces large negative magnetoresistance in the van der Waals semiconductor CrSBr. *Adv. Mater.* **32**, 2003240 (2020).
37. Lee, K. et al. Magnetic order and symmetry in the 2D semiconductor CrSBr. Preprint at http://arxiv.org/abs/2007.10715 (2020).
38. Jungwirth, T., Marti, X., Wadley, P. & Wunderlich, J. Antiferromagnetic spintronics. *Nat. Nanotechnol.* **11**, 231–241 (2016).
39. Jiang, S., Shan, J. & Mak, K. F. Electric-field switching of two-dimensional van der Waals magnets. *Nat. Mater.* **17**, 406–410 (2018).
40. Dash, S. P., Sharma, S., Patel, R. S., de Jong, M. P. & Jansen, R. Electrical creation of spin polarization in silicon at room temperature. *Nature* **462**, 491–494 (2009).
41. Uchida, K. et al. Observation of the spin Seebeck effect. *Nature* **455**, 778–781 (2008).
42. Rameshti, B. Z. & Moghaddam, A. G. Spin-dependent Seebeck effect and spin caloritronics in magnetic graphene. *Phys. Rev. B* **91**, 155407 (2015).
43. Villamor, E., Isasa, M., Hueso, L. E. & Casanova, F. Temperature dependence of spin polarization in ferromagnetic metals using lateral spin valves. *Phys. Rev. B* **88**, 184411 (2013).
44. Nagaosa, N., Sinova, J., Onoda, S., MacDonald, A. H. & Ong, N. P. Anomalous Hall effect. *Rev. Mod. Phys.* **82**, 1539–1592 (2010).
45. Song, G., Ranjbar, M. & Kiehl, R. A. Operation of graphene magnetic field sensors near the charge neutrality point. *Commun. Phys.* **2**, 95 (2019).
46. Mendes, J. et al. Spin-current to charge-current conversion and magnetoresistance in a hybrid structure of graphene and yttrium iron garnet. *Phys. Rev. Lett.* **115**, 226601 (2015).
47. Zhang, Y., Tan, Y.-W., Stormer, H. L. & Kim, P. Experimental observation of the quantum Hall effect and Berry's phase in graphene. *nature* **438**, 201–204 (2005).
48. Tse, W.-K., Qiao, Z., Yao, Y., MacDonald, A. H. & Niu, Q. Quantum anomalous Hall effect in single-layer and bilayer graphene. *Phys. Rev. B* **83**, 155447 (2011).
49. Zhou, B., Chen, X., Wang, H., Ding, K.-H. & Zhou, G. Magnetotransport and current-induced spin transfer torque in a ferromagnetically contacted graphene. *J. Phys. Condens. Matter* **22**, 445302 (2010).
50. Chappert, C., Fert, A. & Van Dau, F. N. *Nanoscience and Technology: A Collection of Reviews from Nature Journals* (ed. Rodgers, P.) 147–157 (World Scientific, 2010).

Methods

Device fabrication. The bilayer graphene and CrSBr flakes were mechanically cleaved from their bulk crystals on SiO_2/Si substrates using adhesive tapes[51]. The bilayer graphene flakes were identified by their optical contrast with respect to the substrate[52]. The thicknesses of the flakes were verified by atomic force microscopy (Supplementary Section 1).

For Device D1, using a dry pick-up technique[53], we transferred the bilayer graphene on the bulk CrSBr flake with a polycarbonate–polydimethylsiloxane stamp. The polycarbonate was removed in chloroform, followed by annealing in an Ar/H_2 atmosphere for 6 h at 350 °C. The preparation of the vdW stack was followed by the fabrication of Al_2O_3(0.8 nm)/Co(30 nm)/Ti(5 nm)/Au(40 nm) electrodes on the vdW stack by an electron-beam lithography technique (using poly(methyl methacrylate) as the electron-beam resist). The Ti/Au layers were deposited on the Co layer for mechanical strength of the contacts and air protection. The exfoliation of all the flakes, atomic force microscopy characterizations and device fabrication were performed under exposure to air (ambient conditions) over a timescale of about seven days.

For device D3 (AHE), the large area bilayer graphene flake on the SiO_2 substrate was initially etched into a Hall-bar geometry in an O_2 plasma environment, using a prepatterned poly(methyl methacrylate) membrane as the mask. The etching procedure was followed by mechanical removal of the poly(methyl methacrylate) membrane to leave the surface of the graphene flake residue free. The bulk CrSBr flake, initially exfoliated on a polydimethylsiloxane stamp, was transferred on top of the etched graphene, partially covering the Hall bar. Device fabrication was completed by the electron-beam lithography of the Ti(5 nm)/Au(100 nm) electrodes, deposited by the electron-beam evaporation of the metals in an ultrahigh vacuum.

Electrical measurements. A low-frequency (<20 Hz) lock-in technique with an a.c. current source up to 10 μA was used for the charge- and spin-transport measurements. For the electrical gating, a Keithley source-meter was used as the d.c. voltage source. The sample was measured in a helium atmosphere in a cryostat with a variable temperature insert and a superconducting magnet. To apply the magnetic field in all possible directions (in-plane and out-of-plane) rotatable sample holders were used.

SQUID measurements. The d.c. magnetic susceptibility was measured in a cryogenic R-700X SQUID magnetometer. The magnetization of a single crystal of CrSBr was measured as a function of the magnetic field, applied in a determined orientation with respect to the crystal axes.

CrSBr synthesis. CrSBr crystals were grown following a modified method developed by Beck[36,54]. S_2Br_2 and Cr powder were loaded in a fused silica tube in a 1.1:2 stoichiometric ratio, and sealed under vacuum. The tube was heated in a multizone tube furnace with a temperature gradient of 1,123 K to 1,223 K for five days. Flat, shiny elongated CrSBr crystals formed in the middle of the tube, with $CrBr_3$ forming at the cold end and Cr_2S_3 at the hot end as side products. The black CrSBr crystals were cleaned with warm pyridine, water and acetone.

Data availability

The authors declare that all data supporting the findings of this study are available within the paper and its Supplementary Information. Any further related information can be provided by the corresponding author upon reasonable request. Source data are provided with this paper.

References

51. Novoselov, K. et al. Two-dimensional atomic crystals. *Proc. Natl Acad. Sci. USA* **102**, 10451–10453 (2005).
52. Li, H. et al. Rapid and reliable thickness identification of two-dimensional nanosheets using optical microscopy. *ACS Nano* **7**, 10344–10353 (2013).
53. Zomer, P. J., Guimarães, M. H. D., Brant, J. C., Tombros, N. & van Wees, B. J. Fast pick up technique for high quality heterostructures of bilayer graphene and hexagonal boron nitride. *Appl. Phys. Lett.* **105**, 013101 (2014).
54. Beck, J. Über chalkogenidhalogenide des chroms synthese, kristallstruktur und magnetismus von chromsulfidbromid, crsbr. *Z. Anorg. Allg. Chem.* **585**, 157–167 (1990).

Acknowledgements

We thank M. H. D. Guimarães and E. J. Telford for discussions and T. J. Schouten, H. Adema, H. de Vries, A. Joshua and J. G. Holstein for technical support. This research received funding from the Dutch Foundation for Fundamental Research on Matter (FOM) as a part of the Netherlands Organisation for Scientific Research (NWO), FLAG-ERA (15FLAG01-2), the European Union's Horizon 2020 research and innovation programme under grant agreements no. 785219 and no. 881603 (Graphene Flagship Core 2 and Core 3), NanoNed, the Zernike Institute for Advanced Materials and the Spinoza Prize awarded in 2016 to B.J.v.W. by NWO. Synthesis, structural characterization and magnetic measurements are supported as part of Programmable Quantum Materials, an Energy Frontier Research Center funded by the US Department of Energy (DOE), Office of Science, Basic Energy Sciences (BES), under award DE-SC0019443. A.H.D. is supported by the NSF graduate research fellowship program (DGE 16-44869).

Author contributions

T.S.G. and B.J.v.W. conceived the project. T.S.G. fabricated the devices and performed the main experiments and data analysis with the help of A.A.K. and supervision of B.J.v.W. A.A.K. performed the analytical modelling. T.S.G. and D.K.d.W. performed the measurements and data analysis of the AHE. A.H.D. and X.R. synthesized the CrSBr crystals and performed the SQUID magnetometry and analysis. T.S.G. wrote the manuscript and Supplementary Information with help from A.A.K. All the authors discussed the results and commented on the manuscript.

Competing interests

The authors declare no competing interests.

Additional information

Supplementary information The online version contains supplementary material available at https://doi.org/10.1038/s41565-021-00887-3.

Correspondence and requests for materials should be addressed to T.S.G.

Peer review information *Nature Nanotechnology* thanks the anonymous reviewers for their contribution to the peer review of this work.

Reprints and permissions information is available at www.nature.com/reprints.